Eur. Phys. J. E **16**, 389–400 (2005)
DOI 10.1140/epje/i2004-10097-9

THE EUROPEAN PHYSICAL JOURNAL E

Direct observation of counterion organization in F-actin polyelectrolyte bundles

T.E. Angelini[1], H. Liang[1], W. Wriggers[2], and G.C.L. Wong[1,a]

[1] Department of Materials Science & Engineering, Department of Physics, Department of Bioengineering, University of Illinois at Urbana-Champaign, IL 61801, USA
[2] School of Health Information Sciences, University of Texas Health Science Center at Houston, 7000 Fannin St., Suite 600, Houston, TX 77030, USA

Received 8 September 2004 and Received in final form 2 November 2004 /
Published online: 18 March 2005 – © EDP Sciences / Società Italiana di Fisica / Springer-Verlag 2005

Abstract. Attractions between like-charged polyelectrolytes have been observed in a variety of systems (W.M. Gelbart, R.F. Bruinsma, P.A. Pincus, V.A. Parsegian, Phys. Today **53**, September issue, 38 (2000)). Recent biological examples include DNA, filamentous viruses, and F-actin. Theoretical investigations on idealized systems indicate that counterion correlations play a central role, but no experiments that specifically probe such correlations have been performed. Using synchrotron X-ray diffraction, we have directly observed the organization of multivalent ions on cytoskeletal filamentous actin (a well-defined biological polyelectrolyte) and found an unanticipated symmetry-breaking collective counterion mechanism for generating attractions. Surprisingly, the counterions do not form a lattice that simply follows actin's helical symmetry; rather, the counterions organize into "frozen" ripples parallel to the actin filaments and form structures reminiscent of charge density waves. Moreover, these 1D counterion charge density waves form a coupled mode with twist deformations of the oppositely charged actin filaments. This counterion organization is not sensitive to thermal fluctuations in temperature range accessible to protein-based polyelectrolyte systems. Moreover, the counterion density waves are "pinned" to the spatial periodicity of charges on the actin filament even if the global filament charge density is varied, indicating the importance of charge periodicity on the polyelectrolyte substrate.

PACS. 82.35.Rs Polyelectrolytes – 82.35.Pq Biopolymers, biopolymerization – 87.16.Ka Filaments, microtubules, their networks, and supramolecular assemblies – 87.64.Bx Electron, neutron and X-ray diffraction and scattering

1 Introduction

Electrostatics in aqueous media is often understood in terms of mean-field theories such as the Poisson-Boltzmann formalism [1–3], in which like-charged objects such as polyelectrolytes, always repel. Indeed, DNA chains in water containing monovalent ions always repel one another. Linearized versions of mean-field theory provide the theoretical underpinning for widely employed tools such as Debye-Hückel theory and DLVO (Derjaguin-Landau-Verwey-Overbeek) theory [4,5] which constitute the usual starting point for understanding charged polyelectrolyte or colloidal systems.

In systems with strong electrostatic interactions (containing, for example, high surface charge densities, multivalent ions, etc.), however, the physics is qualitatively different. Interactions between polyelectrolytes can be controlled by the structure and dynamics of the condensed ions surrounding the polyelectrolyte. It has been recognized for some time that the mean-field Poisson-Boltzmann approach cannot produce attractions unless some form of correlation between counterions is introduced [6–10]. As Kirkwood [11] suggested and Oosawa [12, 13] showed using an approximate analytical model, like-charged attractions between polyelectrolytes may be possible due to the correlated fluctuations of the condensed ion layers around strongly charged polyelectrolytes. A large number of recent theoretical investigations have focused on the existence and form of multivalent-ion–induced like-charge attraction between cylindrical polyelectrolytes [14–44], and on the collapse behavior of the polyelectrolyte itself [45–52]. A number of excellent general reviews have recently been published [53–56].

Like-charge attractions have been experimentally observed in a wide range of polyelectrolyte systems. DNA can be condensed by multivalent ions into dense, ordered

[a] e-mail: gclwong@uiuc.edu

states and is one of the most thoroughly studied systems in this context [57–71]. The volume fraction occupied by condensed DNA within the T4 viral capsid is estimated to be approximately 1/2 [66]. This is indeed a remarkable phenomenon, if one considers the barriers against such condensation, such as the strong electrostatic repulsion between the highly charged sugar-phosphate backbone, the large bending modulus of the DNA double helix, and the loss of configurational entropy of the long DNA molecule. The role of non-specific electrostatic interactions is quite important in DNA condensation. For example, recent experiments on polyamine condensation of DNA have shown that the Raman bands associated with the negatively charged DNA phosphate backbone exhibit significant spectral changes upon condensation, in a sequence-independent way, and indicate that these condensing ions interact with DNA non-specifically [67].

Other, more general, counter-intuitive phenomena such as like-charge attraction and overcharging, which are beyond the explanatory scope of mean-field theories, have been investigated by a large number of theoretical studies, using a wide range of approaches [72–80]. Recently, a number of anionic biopolymers (with persistence lengths of 1 μm or more) have been used as experimental systems for the study of like-charge polyelectrolyte attraction, such as the filamentous bacteriophages, microtubules, and F-actin [81,82]. Due to their large persistence lengths, they can be thought of as idealized rod-like polyelectrolytes, and a number of interesting new effects have been found. For example, in the presence of divalent ions, F-actin progressively condenses into close-packed bundles via an intermediate state comprised of 1D lamellar stacks of liquid-crystalline actin networks [52,83,84]. The dependence of DNA and actin condensation on ion valence, size and structure has been systematically studied experimentally [68,81], and an empirically motivated criterion for the valence dependence has been proposed based on experimental results for "dumbbell" divalent ions [85].

These condensation phenomena are important for a wide range of biological and biomedical processes, such as DNA compaction in bacteria and viral capsids, self-assembly of synthetic gene delivery systems, nucleic acid-protein interactions, cytoskeletal regulation, as well as industrial processes such as multivalent salt-induced condensation of impurities in water treatment, and cellulosic fiber flocculation in paper making. Counterion correlations can also have unexpected applications. For example, the nanometer-scale organization of condensed ions by polyelectrolytes such as DNA may have interesting applications in biomineralization and solution templating [86]. The helical sugar-phosphate backbone of DNA creates a spatially periodic anionic ridge that organizes condensed Cd^{2+} and guides subsequent CdS crystallization.

Although experiments show unambiguously that an attractive interaction exists, there has been little done on measuring actual counterion correlations, which are necessary for generating attractions. Polyelectrolytes in aqueous solution are coated by a condensed "Manning" layer of mobile oppositely charged counterions [51,57]. All proposed theoretical explanations for like-charge attraction introduce some form of positional counterion correlations within this layer. For example, dynamic "van der Waals"-like correlations of long-wavelength ion fluctuations have been suggested [11–13,20,21,23,49]. Static mechanisms consisting of ion correlations along the axis of the polyelectrolyte rods in the form of a Wigner lattice have also been considered [17,19,26,34]. Recently, theoretical models based on discretized distributions of condensed ions on polyelectrolytes have been solved analytically and numerically [24,41–43]. Most theoretical approaches, however, employ idealized models for the polyelectrolytes, such as infinitely thin lines or "smooth" cylinders, or perfect idealized helices. In this work, we aim to measure counterion correlations directly, using a synchrotron X-ray diffraction, and examine the extent to which these predictions survive in a real polyelectrolyte system (as well as how they might be modifed), providing a point of contact between the theoretical viewpoints above.

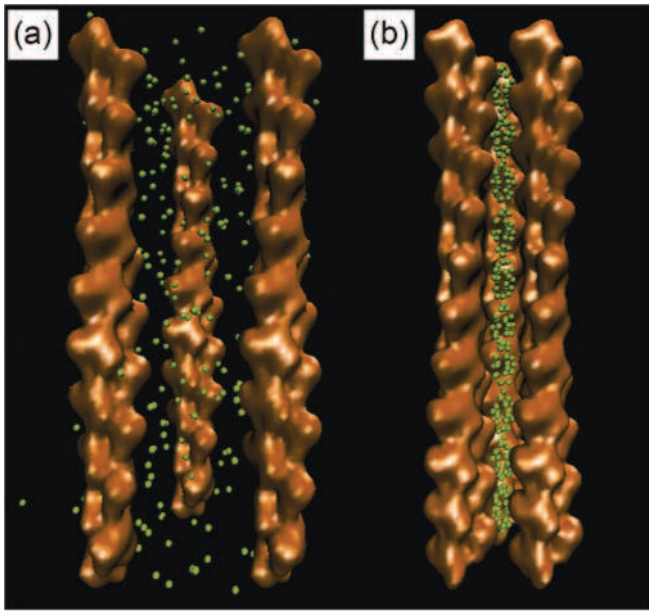

Fig. 1. Schematic representations of uncondensed and condensed F-actin: (a) At low multivalent ion concentrations, three F-actin filaments maintain their native $-13/6$ symmetry, and are unbound. (b) At high multivalent ion concentrations, the ions collectively form a charge density wave (CDW) and "bundle" F-actin filaments. Moreover, the CDW forms a coupled mode with torsional distortions of the F-actin, and has overtwisted it by $-3.8\,^\circ$ per monomer to a new $-36/17$ symmetry. The representations of F-actin are low-resolution density maps generated using situs software (`http://situs.biomachina.org/`).

We examine the organization of multivalent ions on actin filaments (a well-defined, rod-like biological polyelectrolyte) using synchrotron X-ray diffraction, and find a new form of collective counterion correlation [87]. Surprisingly, the counterions do not form a lattice that simply follows actin's helical symmetry; rather, they organize into one-dimensional (1D) charge density waves (CDW)

parallel to the actin filaments (Fig. 1). Moreover, this 1D counterion charge density wave forms a coupled mode with torsional distortions of the oppositely charged polyelectrolyte. This cooperative molecular mechanism is analogous to the formation of polarons in ionic solids, and mediates attractions by facilitating a "zipper-like" charge alignment between the counterions and polyelectrolytes. The counterion mechanism we observe here (and its variations) is applicable to a wide range of colloidal and biomedical processes which depend on controlling interactions between macro-ions dispersed in fluid suspensions.

In a broader perspective, we have shown that it is possible for many actin filaments to collectively twist by *the same amount* in concert, in response to binding by crosslinking agents (divalent ions in the present case). The ramifications of this coupling between filament twist and linker binding are potentially larger. Similar compromises between F-actin twist and F-actin crosslinking by actin binding proteins can influence the hierarchy of existing interactions by local modifications of binding sites, and have important thermodynamic consequences for cytoskeletal regulation [88].

2 Materials and methods

2.1 Small-angle X-ray scattering and helix diffraction

Small-angle X-ray scattering (SAXS) measurements were performed using both an in-house X-ray source as well as beam line 4-2 at the Stanford Synchrotron Radiation Laboratory (SSRL). For the in-house experiments, incident CuKα radiation (λ = 1.54 Å) from a Rigaku rotating-anode generator was monochromatized and focused using Osmic confocal multilayer optics, and scattered radiation was collected on a Bruker 2D wire detector (pixel size = 105 μm). For the SSRL experiments, incident synchrotron X-rays from the BL-4-2 8-pole Wiggler were monochromatized to 8.98 keV using a double-bounce Si(111) crystal ($\lambda = 1.3806$ Å), and focused using a cylindrical mirror. The scattered radiation was collected using a MAR Research charged-coupled device camera (pixel size = 79 μm). The 2D SAXS data from both setups have been checked for mutual consistency.

In general, diffraction features generated by counterion correlations are expected to be weak compared with those generated by biopolymer organization. One approach is to use anomalous scattering to discriminate between counterion scattering and biopolymer scattering [89,90]. We found that for the present protein-based system, an unambiguous interpretation of anomalous scattering is complicated by the intensity changes from accumulated radiation damage due to multiple X-ray exposures at different energies required for anomalous scattering. (We typically take a single exposure for each of our samples.) Comparing different preparations of the same sample in order to minimize radiation damage effects is also not an option, since we find that small changes in the global orientational distribution of the bundles will change the counterion CDW scattering intensity, which make such comparisons unfeasible. Moreover, the counterion CDW peak is relatively small, so mapping out intensity changes in this peak on top of all these effects will lead to new ambiguities.

To detect positional correlations in counterion distributions on the surface of a charged polymer using SAXS, a number of experimental strategies have been employed in the present study. For polyelectrolytes with small diameters and thereby high surface curvatures, or for polyelectrolytes that are very flexible, we hypothesized that counterion correlations will be broken up into small domains, and the resultant diffraction peaks will correspondingly broaden and become difficult to distinguish from the background of scattering, which have a number of contributions, including polyelectrolyte organization and form factor effects. Filamentous actin (F-actin) has been chosen as a model system because it is a rigid polyelectrolyte (persistence length ξ_A = 10 μm) with a large diameter (D_A = 75 Å) [91,92] so that counterion correlations can have the potential to form large domains, and thereby generate sharp, detectable peaks. Because the number of atoms that comprise the charged biopolymer is large compared with the number of counterions, high-molecular-weight counterions (Ba^{2+}) have been used to improve the Z-contrast between counterion scattering and biopolymer scattering. Finally, to further highlight the diffraction features that are generated by the counterions, we have compared the SAXS patterns from F-actin that has been concentrated non-electrostatically (with no added multivalent ions) with F-actin that has been condensed electrostatically by using multivalent ions.

In order to do this experiment, it is necessary to obtain at least partially aligned samples, so that correlations along different directions can be discerned. The best alignment of the F-actin biopolymer is usually achieved in samples with monovalent-ion–based buffers such as those typically employed in typical structural biology experiments, and in non-electrostatically concentrated samples, such as those used in our control experiments. Unlike those samples, however, multivalent ion condensed biopolymer samples typically exhibit poor alignment, because of the existence of strong attractions and the resultant precipitation of the F-actin into a condensed pellet during shear mixing. We mitigated this problem by using a small ($300 \times 300\,\mu m^2$) X-ray beam.

This work aims to measure counterion correlations on the surface of F-actin rods. In order to differentiate between scattering contributions from the counterions and those from F-actin, it is necessary to model the scattering from the F-actin helix. Within the kinematical approximation, an X-ray diffraction pattern is proportional to the modulus-squared of the Fourier transform of a sample's electron density. For example, if the charge density of a line charge is periodic along the z-axis, the diffraction pattern becomes a series of planes, or layer lines, separated in reciprocal space by distances, along q_z, inversely related to the period of real space charge density. For periodic line charges with finite widths (for example, real linear polymers), the intensity of their corresponding layer lines is

modulated along q_r and Ψ (radial and azimuthal reciprocal space coordinates). Many of the important biological polymers (such as DNA, F-actin, filamentous viruses) have helical symmetry, described by the ratio $M = p/s$, where p is the number of monomers per crystallographic repeat and s is the number of helical turns per crystallographic repeat. For an azimuthally averaged collection of periodic linear polymers with helical symmetry $M = p/s$ and repeat distance c, the X-ray scattering amplitude takes the form of layer lines described by

$$G_l(q_r) = \sum_n \sum_j f_j J_n(q_r r_j) \exp\left[i\left(-n\psi_j + \tfrac{2\pi l}{c} z_j\right)\right],$$

where the sum over j includes all subunits of the monomer with coordinates (r_j, ψ_j, z_j) and form factor f_j [93]. The outer sum is over all n subject to the constraint $l = ns + mp$ (the so called selection rule, in which n and m are integers), and J_n is the n-th-order Bessel function of the first kind. Each layer line is centered on $q_z = (2\pi l)/c$. Typically, in modeling diffraction from helical molecules, only the lowest-order Bessel functions are kept in the above sum. This is because the higher order the Bessel function, the weaker the contribution.

Normally, F-actin rods are comprised of G-actin monomers packed into a helix with a $-13/6$ symmetry, or 13 monomers in 6 left-handed helical turns. Each G-actin monomer has dimensions of approximately 55 Å × 55 Å × 35 Å, and is comprised of 4 subdomains. These four subdomains can be approximated as 4 spheres with appropriate radii and molecular weights [93]. Figure 2(a) shows the first nine layer lines of the diffraction pattern of the F-actin helix, calculated employing the above four-sphere model for F-actin using a symmetry of $M = -13/6$. Notice that the $l = 6$ and $l = 7$ layer lines (which come from $n = -1$ and $n = 1$ Bessel functions) are much more intense than the other layer lines. For partially aligned F-actin, these layer lines dominate the diffraction pattern.

True helical macromolecules are, of course, not perfect crystals, and so their diffraction features will not be resolution-limited "Bragg" layer lines. Rather, real molecules exhibit finite domain sizes, yielding diffraction features along q_z with finite widths. In the past, layer lines have been modeled with Gaussian profiles [93,94],

$$\exp\left[-\pi d^2 \left(\frac{2\pi l}{c}\right)^2 \right],$$

where $1/2\pi^{1/2}d$ is the so called "coherence length" of the molecule, due to finite domain sizes.

In order to determine the symmetry associated with the observed diffraction pattern, the model F-actin helix has been continuously twisted and compressed. It turns out that the dominant Bessel functions that contribute the most intensity are essentially the same for all symmetries over a fairly wide range. For example, one can twist away from the native $-13/6$ symmetry by ±10 degrees and the most intense Bessel function contributions remain the same: $n = 0$, 2, 4, 6, -5, -3, -1, 1, and so on. The integer m also has a corresponding conserved pattern. This

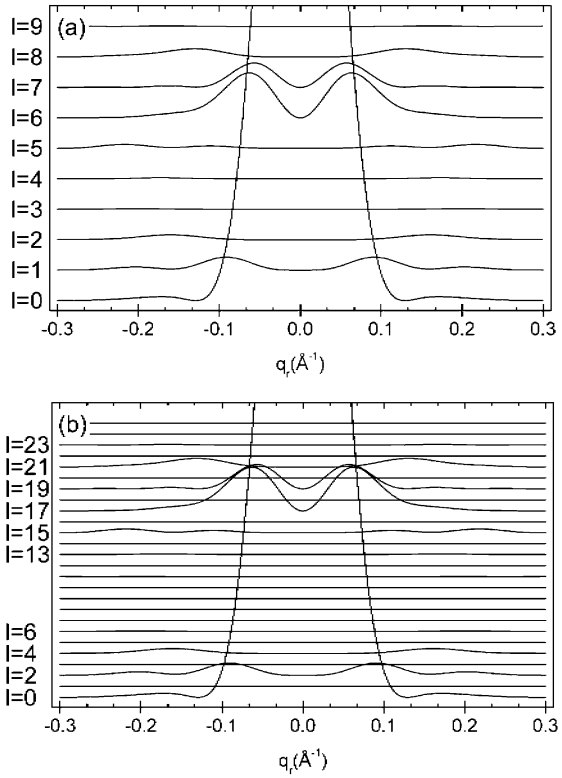

Fig. 2. (a) The scattering amplitude of F-actin with $-13/6$ symmetry, generated using the four-sphere model of the actin monomer. The layer line number is labelled on the left. The most intense areas of the diffraction pattern come from the 0th, 6th, and 7th layer lines with 0th-, and 1st-order Bessel contributions. (b) The equivalent calculation for F-actin with $-36/17$ symmetry. Many more layer lines are generated but most contribute little intensity to the diffraction pattern. As in the $-13/6$ case, the most intense layer lines come from the 0th- and 1st-order Bessel function contributions, this time located at $l = 0$, $l = 17$ and $l = 19$. We only labelled layer lines in (b) that have the same Bessel function contributions as those in (a). For example, $l = 6$ in (b) corresponds to $l = 3$ in (a). This can be shown using the selection rules and the two different symmetries (see text).

point is illustrated by a comparison of Figures 2(a) and 2(b), in which two diffraction patterns corresponding to two different symmetries ($-13/6$ and $-36/17$) with very different length repeat units reveal that the relevant contributions to both diffraction patterns come from the same series of Bessel functions (same combinations of n and m). The continuous twisting and squeezing of the helix can be more conveniently accomplished by re-expressing l and c in the calculation. For example, l only appears in the calculation when a position along q_z is specified. Usually written as $q_z = (2\pi l)/c$, one can use the selection rule to rewrite $q_z = [2\pi(ns/p + m)]/c'$. The axial monomer spacing, c', is given by $c = pc'$. Modeled diffraction patterns can then be calculated by changing the helical symmetry and monomer spacing, p/s and c', by *arbitrary* amounts. Figure 3 shows two powder-averaged calculations of the diffraction pattern from the four-sphere model of F-actin

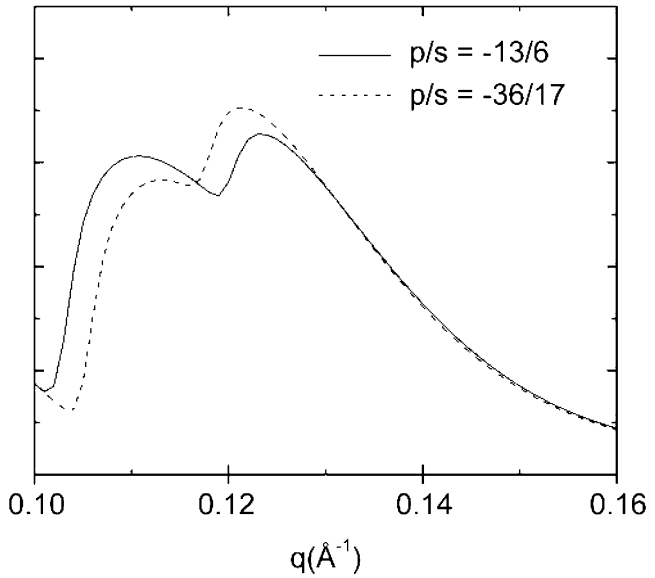

Fig. 3. A sample calculation of powder-averaged layer lines for two different filament symmetries. The $l = 6$ and $l = 7$ layer lines are shown for the $-13/6$ case and the $l = 17$ and $l = 19$ layer lines are shown for the $-36/17$ case. Both symmetries have the same Bessel function contributions ($n = -1$ for the lower-order line and $n = 1$ for the higher-order line). Inclusion of extra neighboring layer lines has no effect on peak position and a negligibly small effect on peak width. Changing the filament symmetry will lead to changes in peak position and relative intensities; shown here are the two symmetries yielding peak positions closest to our measurements (see Fig. 5) $-13/6$ (0.111 Å^{-1} and 0.123 Å^{-1} in exact agreement with peaks D and E in Fig. 5) and $-36/17$ (0.113 Å^{-1} and 0.121 Å^{-1} in excellent agreement with peaks J and K in Fig. 5).

for two different symmetries ($-13/6$ and $-36/17$, corresponding to the native state of the F-actin and an overtwisted state with a twist of $-3.8\,^\circ$ per monomer).

2.2 Sample preparation

The most abundant intracellular protein in eukaryotic cells is actin, one of the principal components of the cytoskeleton. Actin associates to form polymeric actin filaments, which can in turn form bundles and networks in a highly coordinated way by interacting with actin binding proteins and salts. The actin cytoskeleton determines cell shape, and plays a central role in cellular locomotion [91]. Monomeric actin (G-actin) (molecular weight, 43000) was prepared from a lyophilized powder of rabbit skeletal muscle purchased from Cytoskeleton (Denver). The non-polymerizing G-actin solution contained a 5 mM Tris buffer at *p*H 8.0, with 0.2 mM $CaCl_2$, 0.5 mM ATP, 0.2 mM DTT, and 0.01% NaN_3. G-actin (2 mg/ml) was polymerized into F-actin (linear charge density $\lambda_A \approx -1e/2.5$ Å at *p*H 7) with the addition of salt (100 mM KCl final concentration). Samples were typically polymerized for 1 hour. Human plasma gelsolin, an actin severing and capping protein (`Cytoskeleton.com`), was used to regulate the F-actin length. The average length of F-actin is controlled by the gelsolin concentration, which has been independently calibrated [95]. The filaments were treated with phalloidin (molecular weight 789.2) to prevent actin depolymerization. F-actin gels were ultracentrifuged at $100000 \times$ g for 1 hour to pellet the filaments. After the removal of the supernatant buffer solution, the F-actin was resuspended to a final concentration of 10 mg/ml by using Millipore H_2O (18.2 MΩ). Electrostatically concentrated samples were prepared by mixing with $MgCl_2$or $BaCl_2$salt solutions. Non-electrostatically condensed samples were prepared by ultracentrifugation ($100000 \times$ g) of F-actin solutions. The supernatant buffer was subsequently removed, and the actin concentration set by the addition of 5 mM *p*H 7.0 Pipes buffer. All samples were sealed in 1.5 mm diameter quartz capillaries.

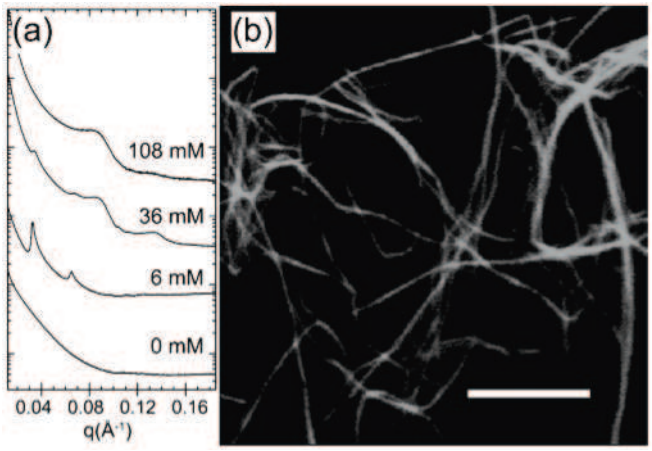

Fig. 4. (a) SAXS profiles of F-actin (~ 0.2 μm long) condensed by Ba^{2+} ions. At 0 mM Ba^{2+} concentration, F-actin is in an uncondensed isotropic phase. At low Ba^{2+} concentrations (6 mM), F-actin condenses into a network phase, consisting of lamellar stacks of 2D nematic layers (see text). At high Ba^{2+} concentrations (108 mM), an attractive force condenses F-actin into close-packed bundles with a correlation peak at $q = 0.089$ Å^{-1}. A weak higher-order reflection can also be observed at $q = 0.136$ Å^{-1}, which deviates slightly from the position expected from an exact hexagonal lattice. (b) A confocal image of a dilute (0.03 mg/ml) solution of bundles of F-actin (~ 10 μm) at 72 mM global Ba^{2+} concentration. The scale bar is 8 μm.

3 Results and discussion

The basic supramolecular structure of the biopolymer component of the composite counterion-biopolymer system can be seen in the progressive formation of F-actin bundles with increasing multivalent ion concentrations. SAXS measurements of F-actin condensed with Ba^{2+}(Fig. 4(a)) exhibit its structural evolution with increasing Ba^{2+} concentration. At low ion concentrations (for example, 6 mM), F-actin is observed to assemble into a network phase consisting of 1D lamellar stacks of

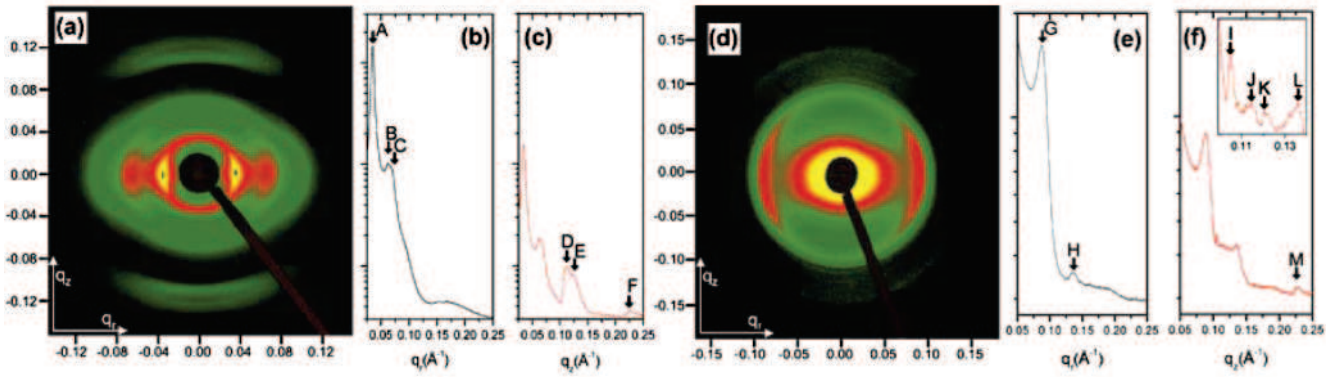

Fig. 5. (a) A 2D SAXS pattern of non-electrostatically condensed F-actin. The procedure for generating integrated cuts along q_r (b) and along q_z (c) are described in the text. Peak positions for all observed layer lines (6th, 7th, and 13th) agree with the native $-13/6$ actin model to within less than 1%. (d) 2D SAXS of Ba^{2+}-condensed F-actin. Cuts along q_r (e) and along q_z (f) are performed the same way. The data indicates the formation of a counterion 1D CDW, and an induced $-3.8\,^\circ$ overtwist of F-actin (see text). The peak positions are 0.035 Å^{-1} (A), 0.062 Å^{-1} (B), 0.07 Å^{-1} (C), 0.111 Å^{-1} (D), 0.123 Å^{-1} (E), 0.225 Å^{-1} (F), 0.089 Å^{-1} (G), 0.136 Å^{-1} (H), 0.105 Å^{-1} (I), 0.115 Å^{-1} (J), 0.120 Å^{-1} (K), 0.136 Å^{-1} (L), and 0.227 Å^{-1} (M). The inset is a magnification of the CDW peak (I) and neighboring layer line scattering (J, K).

2D nematic layers of actin filaments [83]. At intermediate Ba^{2+} concentrations (*e.g.*, 36 mM) a second set of peaks emerges, indicating coexistence between the network phase and uniaxial bundles. At even higher Ba^{2+} concentrations all indications of the network phase have disappeared, and we see an actin-actin close-packing peak characteristic of the bundled phase at $q = 0.089$ Å^{-1}, which corresponds approximately to the hard-core diameter of F-actin. These F-actin bundles can also be imaged in real space by using laser-scanning confocal fluorescence microscopy (Fig. 4(b)). The F-actin filaments were labeled with phalloidinated Alexa Fluor 488 (Molecular Probes). A Leica SP-2 confocal microscopy system (Beckman Institute, Urbana, IL) was used to image the dilute F-actin solutions in sealed sample cells at different ionic strengths. The observed thickness of bundles in the image, accounting for the ~ 0.25 μm point spread function of the microscope, indicates that each bundle is comprised of thousands of filaments (assuming that the actin filaments are close-packed at the spacing indicated by the X-ray results).

A direct comparison between the 2D SAXS patterns of F-actin concentrated osmotically without using divalent ions and of F-actin condensed electrostatically with divalent ions is made in Figure 5. A large number of different osmotically concentrated F-actin samples were analyzed. Figure 5(a) is a representative 2D SAXS pattern of partially aligned F-actin at 90 mg/ml in the absence of divalent ions. The F-actin rods are partially aligned along the q_z-axis and are powder-averaged in the plane perpendicular to the q_z-axis. In the region of interest in reciprocal space the small-angle approximation is valid, so the relationship between detector positions and q positions is greatly simplified. For the analysis of the 2D SAXS patterns (Figs. 5(a) and (d)), cuts along q_r and q_z are produced by integrating the 2D SAXS image over $40\,^\circ$ wedges in χ (χ is the angle between q and q_r), centered about the q_r and q_z axes, where $q_r \equiv q\cos\chi$, $q_z \equiv q\sin\chi$, $q = (4\pi/\lambda)\sin\theta$, and 2θ is the Bragg angle. This numerical "wedge" integration was performed using the standard Fit2D software (`http://www.esrf.fr/computing/scientific/FIT2D/`). The three equatorial peaks (A–C) in Figure 5(b) correspond to the first-order, $\sqrt{3}$-order, and second-order peaks expected from local hexagonal coordination. The two strong, partially orientationally averaged peaks (D and E) along the meridional direction (Fig. 5(c)) are the well known sixth- and seventh-layer lines characteristic of $-13/6$ symmetry [96], in agreement with the known structure of the F-actin. To account for the sample mosaic and the effects of integration on layer lines, we partially powder-averaged ($\pi/2 \geqslant \chi \geqslant \pi/4$) theoretical 2D diffraction patterns. The resulting modeled peak positions have been optimized by varying the monomer spacing in 0.1 Å increments. These peak positions and combined full width at half maximum are well described (to within 1%) by equations (1) and (2) (above) utilizing the Fourier transform of the standard four-sphere model [93] for the actin filament, and using the Holmes coordinates [96] combined with Gaussian layer line profiles [94]. These model 2D diffraction patterns are turned into one-dimensional powder averages produced by numerically integrating over the χ-angle. Two of these model diffraction patterns are presented in Figure 3. The difference between a partial powder average ($\pi/2 \geqslant \chi \geqslant \pi/4$) and a full powder average has no effect on the resulting peak positions as long as most of the layer line intensity is included in the integral.

The diffraction pattern for multivalent ion condensed F-actin bundles differs dramatically from that of the non-electrostatically concentrated F-actin. Figure 5(d) is a 2D SAXS pattern of a partially aligned sample of F-actin at 7.5 mg/ml condensed with 60 mM Ba^{2+}. The filaments are oriented parallel to q_z on average as in the non-electrostatically concentrated sample above. The most salient difference between the two diffraction patterns (between Fig. 5(a) and (d) and between Fig. 5(c)

and (f)) is the appearance of a sharp diffraction feature at $q_z = 0.105$ Å^{-1} in the electrostatically condensed case (Fig. 5(f), peak I). This finding is surprising because the sample alignment is weaker for the electrostatically condensed actin compared with the non-electrostatically condensed actin, and weaker alignment can only broaden and weaken existing peaks, but never produce new ones.

This peak is centered on the q_z-axis and, given the symmetry of the system, is dominated by a 0th-order Bessel function contribution, and is partially smeared in χ. Using the definition of layer line positions given above, one can calculate all possible positions of layer lines with 0th-order Bessel function contributions: $q_{z0} = 2\pi m/c'$. No plausible changes in symmetry can produce new layer lines with 0th-order Bessel function contributions. (In principle, it may be possible to generate a diffraction peak at this position if one were to *double* the the monomer spacing along a filament, but this will no longer be anything resembling an F-actin helix. It is therefore not possible to generate this new peak by using the F-actin helix. This new diffraction peak, which only occurs for multivalent ion condensed samples and is aligned along the q_z-axis, corresponds to "ripples" of multivalent ion density along the filament axis, analogous to a classical 1D charge density wave (CDW). Compared to any of the F-actin layer line peaks in this region of reciprocal space, this peak is symmetrical, significantly sharper, and more intense. This peak is consistent with the diffraction from a new 1D periodic charge distribution with a finite in-plane width and azimuthal symmetry. The Fourier transform of this charge distribution is a periodic arrangement of Bragg sheets multiplied by 0th-order Bessel functions centered on the q_z-axis, which suppress the off-axis Bragg sheet intensity. Unlike the higher-order Bessel function peaks from the F-actin helix, which are shifted and broadened along q_z by the large mosaic distribution of bundle orientations within the sample volume, this peak remains sharp along q_z even after such orientational averaging. Because we observe a single peak, the counterion CDW is dominated by one Fourier component and is approximately described by a simple sinusoidal density variation with a spatial period of 59.8 Å, which is comparable to the spacing between monomer ridges on the surface of one side of an F-actin filament. (This is similar to the density modulation observed in most mesogenic smectic liquid crystals, which also exhibit a single order of diffraction.) Because of the weak diffraction signal of the CDW, we cannot rule out the possibility of higher harmonics, which can also be suppressed by Debye-Waller factors and other effects. Our results, however, suggest that the dominant Fourier component of the CDW is the one at $q_z = 0.105$ Å^{-1}, which implies that the counterion distribution can be approximated by a "frozen" 1D sinusoidal ripple along the F-actin helix axis. In samples where divalent ions are progressively removed from the F-actin bundles, the CDW diffraction feature disappears. We recently performed experiments in which the condensed divalent ions are displaced by titrating in low-molecular-weight multivalent globular proteins such as lysozyme (+9 charge). As the divalent ions in the CDW are displaced by the higher-valence lysozyme, the CDW scattering signal is suppressed as expected [97].

This simple picture, however, is incomplete. For example, why do the counterions follow a new 1D symmetry rather than the full helical symmetry of the charge distribution on F-actin? In principle, if the positively charged divalent ions were to simply follow the negative charge on F-actin, the ion distribution should precess helically with the same symmetry of the F-actin helix, and modify the existing Bessel function scattering and generate no new peaks. This is clearly not the case, since we clearly observe the CDW diffraction peak centered on the q_z-axis. The question can be resolved if we examine the diffraction pattern from the multivalent ion-condensed F-actin, which reveals that the 1D CDW has enforced a change in the native F-actin symmetry and overtwisted the F-actin helix by $-3.8\,^\circ$ per monomer. This can be seen by the direct comparison of Figure 5(d) with the non-electrostatically concentrated actin in Figure 5(a). The equatorial peak positions (G and H) deviate slightly from those expected from an exact hexagonal lattice and indicate that the bundled filaments are tightly packed (Fig. 5(e)). Along the meridional direction, the Bessel function peaks of the native 13/6 layer lines of the non-electrostatically concentrated sample (Fig. 5(c)) have been replaced by a cluster of weaker peaks (J–L) in the multivalent ion condensed sample (Fig. 5(f)). The peak at 0.136 Å^{-1} (L) is clearly caused by the mosaic smearing of the strong transverse inter-rod correlation at the same q-value along the equatorial direction, and the intensity agrees well with calculations accounting for the mosaic distribution. The remaining peaks can be completely explained by overtwisting F-actin to a new $-36/17$ symmetry, which corresponds to the $3.8\,^\circ$ twist. Experimentally, F-actin is known to exhibit a range of twists states [92,98,99], an observation that is consistent with its low torsional rigidity, as measured with single-molecule techniques [100]. We consider changes in the F-actin helical twist away from its native symmetry by starting with the standard four-sphere model in the $-13/6$ helix and monomer spacing of 28.7 Å (the value extracted from the measurement of actin in Fig. 5(a)) and twisting the filament over a range of $\pm 10\,^\circ$ per monomer in increments of $0.05\,^\circ$. Long repeat helical symmetries up to the 108/51 range have been checked for the appearance of new intense layer lines, and none were found. The measured peaks at $q = 0.115$ and 0.120 Å^{-1} agree well with the $l = 17$ and 19 layer lines of the overtwisted $-36/17$ symmetry (calculated peaks at $q = 0.113$ and 0.120 Å^{-1} after adding mosaic smearing). Even the higher-order feature at $q = 0.227$ Å^{-1} is reproduced.

Why does the composite polyelectrolyte-counterion system choose the overtwisted $-36/17$ symmetry? The angle between adjacent monomers on a $-13/6$ helix is given by $-6{*}2\pi/13$, or $-166.2\,^\circ$. By contrast, the angle per monomer on a $-36/17$ helix is $-170\,^\circ$, which indicates the overtwist of $-3.8\,^\circ$ per monomer. An examination of the local environment around a 1D CDW reveals why the $-36/17$ symmetry is favored. Consider a simple columnar hexagonal array of F-actin filaments

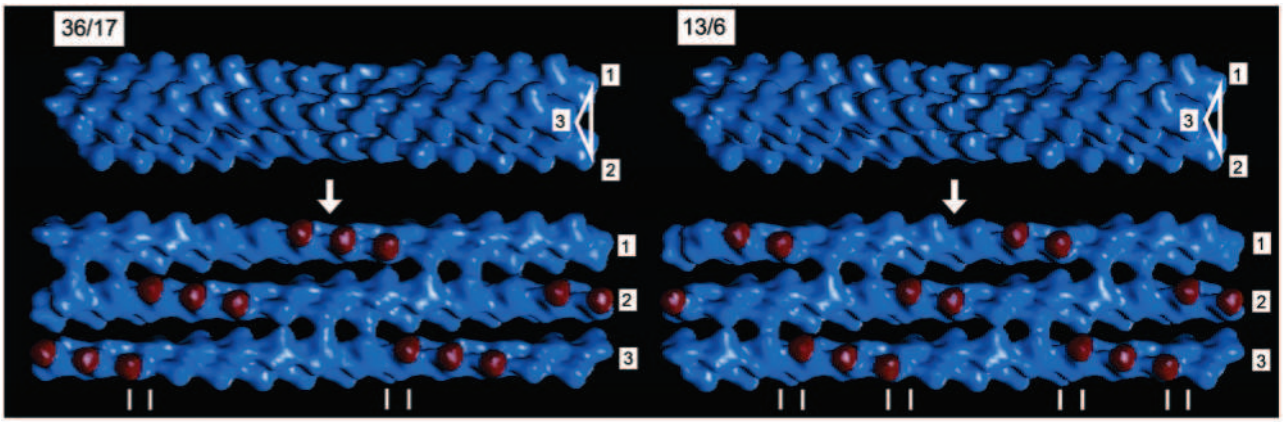

Fig. 6. For the −36/17 and −13/6 symmetries, a schematic representation of a three-filament bundle with the central triangular tunnel highlighted (top) and the same bundle in its "unwrapped" form, showing the interior charge distribution of the tunnel (bottom). The black-colored (red-colored online) regions on each filament correspond to the highly charged sd-1s of the actin monomers facing the interior of the bundle. Double lines mark the location of the electrostatic/steric defects where sd-1s from adjacent filaments are in close proximity. Overtwisting the 13/6 helix to a 36/17 helix dramatically reduces the density of these defects, and generates long regions of evenly spaced charged patches to match with the periodic counterion CDW.

decorated by parallel 1D CDWs. The most elementary unit of this structure is a three-filament bundle, which defines a "channel" of triangular cross-section, threaded by a 1D CDW of ions. Figure 6 depicts the negative charge distribution within such a three-filament bundle. The black-colored (red-colored online) regions on each filament correspond to subdomain-1s (sd-1s) of the actin monomers that face the inside of the channel. These subdomains are the most highly negatively charged and the most protrusive regions on the surface of F-actin. To lower the electrostatic energy, these domains should ideally be positioned adjacent to the maxima of the oppositely charged 1D CDW. However, because F-actin is a helix, the highly charged sd-1 will precess in and out of this central channel and will not always be in register with the CDW. If we examine the "unwrapped" three-filament bundle and look at the distribution of negative charge on the surface of the "channel", following sd-1 from monomer to monomer and filament to filament along the bundle, we find that no matter how the initial relative phases of the F-actin are chosen, a large number of defects will occur for the native −13/6 symmetry, in which sd-1s of adjacent filaments are in very close proximity to one another, which is electrostatically and sterically unfavorable. Given that F-actin is a helix, defects of this kind are unavoidable, unless the helix was completely unwound, which is clearly unrealistic. However, it can be seen that the spatial frequency of these defects is dramatically reduced if the F-actin filament is overtwisted to a −36/17 symmetry. The −36/17 symmetry provides regions with evenly spaced negative-charge patches with a period equal to twice the monomer spacing on a single filament, $d = 57.4$ Å, which is quite close to 59.8 Å, our measured period for the 1D CDW of multivalent ions. In fact, this observed organization of multivalent ions into a classical CDW may be related to the occurrence of these defects. It is interesting to note that the occurrence of these mismatch defects, which will always occur for a columnar lattice of helical rods, do not destroy the counterion CDW, and that the CDW peak remains sharp.

It is not intuitively obvious that by optimizing the electrostatic interactions in a single interstitial channel will necessarily do so for all of the interstitial channels. F-actin is a helix, and the charged patches will precess with a spatial frequency determined by its helical symmetry. As a result, optimizing the charge matching for a CDW threading one "channel" will not in general optimize charge matching in adjacent "channels', due to frustration effects. An examination of this question reveals one other important advantage in changing the actin twist state from −13/6 to −36/17. There are 36 monomers in the crystallographic repeat of twisted F-actin in the −36/17 configuration. The 36 monomers are evenly divisible by 6, the number of nearest neighbors, whereas 13, the number of monomers in the native crystallographic repeat of F-actin, is not (Fig. 7). For F-actin rods with −36/17 symmetry organized into a 6-fold columnar arrangement, all of the interstitial channels can be optimized simultaneously. A unit cell can be generated with two principal channel arrangements that can be simultaneously optimized, and the entire 2D plane can be tiled with a unit cell without frustration effects (only one of the two possible channel types are shown in Fig. 6). This is clearly not true for −13/6 F-actin, for which it is not possible to tile the 2D surface without frustration.

Recent molecular-dynamics simulations on realistic representations of F-actin at a spatial resolution comparable to the actin monomer subdomain structure confirm the essential features of our model [101]. For a columnar hexagonal lattice comprised of F-actin helices in the native −13/6 twist state, counterions are distributed around F-actin with the symmetry of individual actin helices, while for a lattice of F-actin in the −36/17 twist state, counterion distributions rearrange themselves to follow

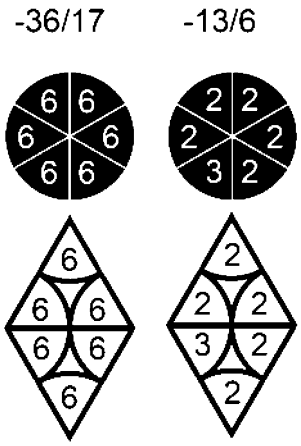

Fig. 7. The projection of the F-actin filament into a plane perpendicular to the filament axis reveals the relationship between filament symmetry and inter-filament coordination. The number of monomers per repeat length oriented within each of the six 60° sectors are shown on each sector (top diagrams). For example, with the −36/17 symmetry, there are 36 monomers per repeat, and they evenly divide into six monomers per 60° sector. In the −36/17 case (left), each of the six nearest neighbors facing the filament will interact with the same number of monomers per repeat length. On the other hand, a filament with −13/6 symmetry (right) will always have one neighbor inequivalent to the rest. This will have fundamental consequences for hexagonal packing (bottom diagrams). For filaments with −36/17 symmetry organized into a hexagonal columnar arrangement, all the channels can be optimised against the CDW simultaneously. In contrast, filaments with −13/6 symmetry in the same columnar arrangement will have channels that cannot be simultaneously optimised.

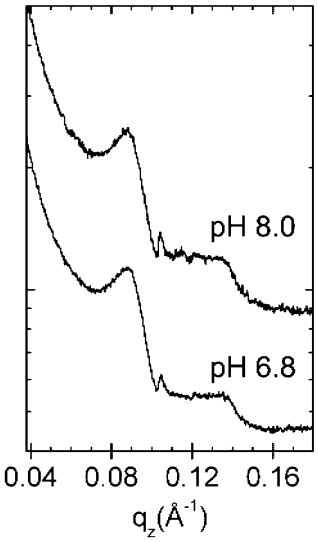

Fig. 8. SAXS intensity for 7.5 mg/ml F-actin, 2 μm in length, at two *p*H levels: both samples contained 80 mM Ba^{2+}. The low *p*H sample was prepared in Pipes buffer, the high *p*H sample was prepared in Hepes buffer. Over a $\sim 6\%$ change in charge density, the filament packing is observed to be the same in both cases, and the CDW peak does not shift at all, illustrating that the period of the CDW is not dependent upon the average underlying filament charge density, but on the geometric arrangement of charge within the bundle. Poor sample alignment has washed out the separation between the broad layer lines from filament scattering, but the CDW peak remains sharp.

the symmetry of the hexagonal lattice. This supports the experimental observation of a strong CDW state for twisted −36/17 F-actin rods.

It is important to assess whether the $-3.8\,^\circ$ twist necessary for the fomation of the −36/17 helix is forbiddingly large. The torsional rigidity of F-actin has been measured [100]. By using the measured value for the torsional rigidity ($\kappa \approx 8 \times 10^{-26}$ Nm^2) and the equipartition theorem, the rms twist of F-actin at room temperature just from thermal fluctuations is of the order 1° per monomer.

If the counterion CDW is in registration with the pattern of charges defined by the twisted F-actin rods, then its spatial periodicity must remain constant as long as the structure of F-actin is preserved, even if the linear charge density of the F-actin were varied, and concomitantly, the number of condensed ions. We checked this possibility by exploiting the four histidine residues on the G-actin monomer. The protonation of histidines can be controlled by the *p*H of the solvent. As the *p*H is changed between 6 and 8, the charge density on the actin rod changes by $\sim 20\%$. We changed the charge density of the actin filament between *p*H 6.8 and 8.0 (Fig. 8), and observe no shift in the position of the CDW diffraction peak, as expected. This indicates that the charge modulation of the CDW is not affected by the underlying *average* charge density. Rather, the CDW is "pinned" because of the geometric arrangement of charge (and defects) on the filaments. It is possible, however, that the average inter-ion spacing is changing as the charge density of F-actin is varied, but we cannot at present measure the inter-ion correlations to confirm this. The CDW diffraction peak is associated with organization of the ions at a larger length scale than inter-ion correlations.

Ion specificity has important implications in biology, so the question arises whether the CDW is a Ba^{2+} specific phenomenon. All of the multivalent ion/F-actin self-assembled phases have been observed in the past using a variety of ion species such as Mg^{2+} and Ca^{2+} [83]. In agreement with these findings, we observe the CDW peak in SAXS measurements on partially aligned samples of actin condensed by Mg^{2+} and by Ca^{2+} (Fig. 9). These measurements were performed under conditions identical to those of the Ba^{2+} measurements, and the CDW peak is weaker than that for Ba^{2+} in both cases. The above observations indicate that the CDW state is not limited to Ba^{2+}-condensed actin bundles, and suggest that it is due to a collective ion organization rather than to ion-specific binding phenomenon. Although there are approximate trends in the CDW peak intensities for different ion species (*e.g.*, the Ca CDW peak appears more intense than the Mg CDW peak in Fig. 9, etc.), they are difficult to quantitatively compare due to the uncontrollable affects of mosaic smearing within only partially aligned samples, and to the shifts in phase boundaries between

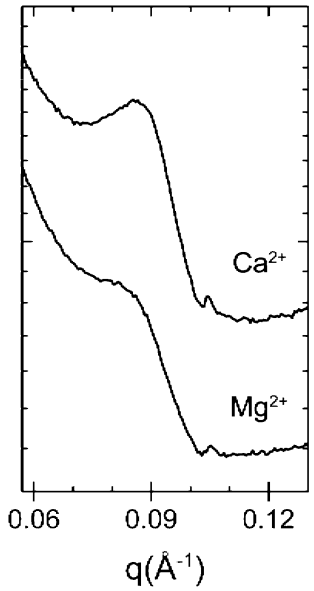

Fig. 9. SAXS intensity for 7.5 mg/ml F-actin, 2 μm in length, condensed by 80 mM Mg^{2+} and 80 mM Ca^{2+}. Both samples were prepared in 5 mM Pipes buffer at *p*H 7. The same structure here is observed as in the case of Ba^{2+}. The peak at 0.089 $Å^{-1}$ is the close-packing peak, and the small peak at 0.105 $Å^{-1}$ is the CDW peak. The existence of the CDW for Mg^{2+} and Ca^{2+} in addition to Ba^{2+} indicates the non-specific nature of the CDW. Poor sample alignment washes out layer lines, so filament twist information cannot be extracted.

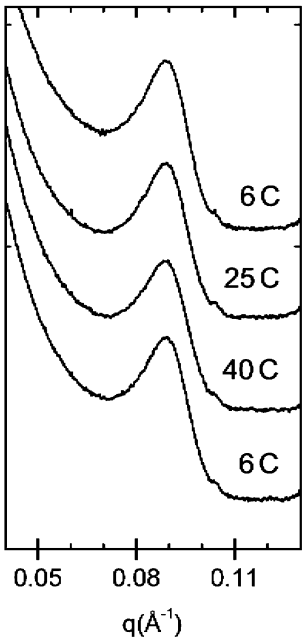

Fig. 10. SAXS measurements for 7.5 mg/ml F-actin, 10 μm in length, condensed by 90 mM Ba^{2+} in 5 mM Pipes buffer at *p*H 7. The peak positions, widths, and intensities did not change as the temperature was varied, indicating that the bundles did not swell or shrink, nor did domain size within bundles significantly change. In order to account for any radiation damage incurred during the measurements, we measured first at 6 °C, then at 25 °C, then at 40 °C, and finally at 6 °C again. The nearly identical intensity profiles from the two 6 °C measurements indicates that no significant radiation damage was sustained by the sample.

different condensed phases for different ions [83] (which can potentially vary the number of condensed ions on the polyelectrolyte for a given global ion concentration). What's more, since anionic actin filaments are comprised of large numbers of both cationic as well as anionic residues, coions may co-organize with counterions on the actin surface and contribute to the diffraction signal. For example, in our system we have Cl co-ions, which have a Z that is greater than that of Mg and less than those of Ca and Ba. This will impinge strongly on the relative peak intensities and significantly diminish the differences between the CDW diffraction signals from different salts like $MgCl_2$, $CaCl_2$ and $BaCl_2$.

It is interesting to assess how the CDW organization changes with respect to thermal fluctuations. All measurements presented above were performed at room temperature. Figure 10 shows a series of SAXS measurements performed on bundles of F-actin condensed with 90mM Ba^{2+}, at temperatures ranging from 6 °C to 40 °C. (The temperature range was chosen for practical purposes; we did not go below the freezing point of water, or above 40 °C to avoid denaturing actin.) The sample was allowed to equilibrate for 1 hour at each temperature point before measurements, and the samples were always cycled to the original temperature to check to reproducibility and possible beam damage. The bundles do not exhibit any discernable structural changes with temperature. The peaks are not observed to shift, so bundles do not swell or shrink over this temperature range. Changes in peak widths are not observed and changes in peak intensities are negligible, indicating that the average domain size within the bundles does not change significantly at the temperature range probed.

The possibility of coupling between the CDWs in neighboring tunnels deserves comment. For example, do the 1D CDWs exist in isolation, or are they locked into a 2D lattice via interactions with the columnar lattice of F-actin rods? In principle, an X-ray lineshape measurement may be able to differentiate between the possibilities. However, there is not sufficient dynamic range in the diffraction signal to detect inter-CDW coupling, by discriminating between true long-range order (LRO), which is expected if the CDWs in different channels are coupled, and quasi-LRO (QLRO), which is expected from an uncoupled 1D system of finite extent (and therefore capable of bending and compression) [102]. In fact, the peaks are expected to be sharp for both LRO and QLRO. For example, the diffraction peaks for the 1D density wave in smectic liquid crystals are frequently resolution-limited in width, and the differences are detected usually in the asymptotic behavior of the correlation peaks [103,104].

4 Conclusions

We have experimentally examined the mechanism for like-charge attraction in cytoskeletal F-actin and found evidence for counterion correlations. The microscopic mechanism involves a coupled mode between a counterion CDW and the polyelectrolyte twist. (The counterion CDW cannot exist without the polyelectrolyte twist and vice versa.) This molecular mechanism may be analogous to the formation of polarons in ionic solids, in which an electron drags a "cloud" of longitudinal optic phonons and acquires a large effective mass [105,106]. In a broader context, similar collective compromises between F-actin twist and crosslinking of F-actin by actin binding proteins may influence the hierarchy of existing interactions [88] and have important thermodynamic consequences for cytoskeletal regulation. Another general issue is the role of ion multivalence in like-charge attraction, because different polyelectrolytes require ions of different valences to condense. An experimentally motivated criterion for the degree of ion multivalence required for generating attractions has been recently proposed [85], and a systematic study of collective counterion dynamics for different ion valences is under way.

We are grateful to K. Schweizer and K. Schulten for helpful discussions. This work is based in part upon work supported by the U.S. Department of Energy, Division of Materials Sciences, under Award No. DEFG02-ER9645439, through the Frederick Seitz Materials Research Laboratory at the University of Illinois at Urbana-Champaign, and by NSF DMR-0409369. Research for this publication was carried out in the Center for Microanalysis of Materials, University of Illinois at Urbana-Champaign, which is partially supported by the U.S. Department of Energy under grant DEFG02-91-ER45439.

References

1. J. Israelachvili, *Intermolecular and Surface Forces*, 2 ed. (Academic Press, London, 1992).
2. D.R. Evans, H. Wennerstrom, *The Colloidal Domain*, 2 ed. (Wiley, New York, 1999).
3. P. Nelson, *Biological Physics* (Freeman, New York, 2004).
4. B.V. Derjaguin, L. Landau, Acta Physicochim. (URSS) **14**, 633 (1941).
5. E.J. Verwey, J.T.G. Overbeek, *Theory of the Stability of Lyophobic Colloids* (Elsevier, Amsterdam, 1948).
6. M. LeBret, B.H. Zimm, Biopolymers **23**, 287 (1984).
7. L. Guldbrand, L. Nilsson, L. Nordenskiöld, J. Chem. Phys. **85**, 6686 (1986).
8. C.F. Anderson, M.T. Record jr., Annu. Rev. Biophys. Chem. **19**, 423 (1990).
9. G. Lamm, L. Wong, G.R. Pack, Biopolymers **34**, 227 (1994).
10. L.G. Nilsson, L. Guldbrand, L. Nordenskiöld, Mol. Physiol. **72**, 177 (1991).
11. J.G. Kirkwood, J.B. Shumaker, Proc. Natl. Acad. Sci. U.S.A. **38**, 863 (1952).
12. F. Oosawa, Biopolymers **6**, 1688 (1968).
13. F. Oosawa, *Polyelectrolytes* (Marcel Dekker, New York, 1971).
14. J. Ray, G.S. Manning, Langmuir **10**, 2450 (1994).
15. A.P. Lyubartsev, L. Nordenskiöld, J. Phys. Chem. **99**, 10373 (1995).
16. A.P. Lyubartsev, L. Nordenskiöld, J. Phys. Chem. B **101**, 4335 (1997).
17. I. Rouzina, V.A. Bloomfield, J. Phys. Chem. **100**, 9977 (1996).
18. I. Rouzina, V.A. Bloomfield, Biophys. Chem. **64**, 139 (1997).
19. N. Grønbech-Jensen, R.J. Mashl, R.F. Bruinsma, W.M. Gelbart, Phys. Rev. Lett. **78**, 2477 (1997).
20. B.-Y. Ha, A.J. Liu, Phys. Rev. Lett. **79**, 1289 (1997).
21. B.-Y. Ha, A.J. Liu, Phys. Rev. Lett. **81**, 1011 (1998).
22. R.M. Nyquist, B.-Y. Ha, A.J. Liu, Macromolecules **32**, 3481 (1999).
23. R. Podgornik, V.A. Parsegian, Phys. Rev. Lett. **80**, 1560 (1998).
24. F.J. Solis, M. Olvera de la Cruz, Phys. Rev. E **60**, 4496 (1999).
25. A.P. Lyubartsev, J.X. Tang, P.A. Janmey, L. Nordenskiöld, Phys. Rev. Lett. **81**, 5465 (1998).
26. B.I. Shklovskii, Phys. Rev. Lett. **82**, 3268 (1999).
27. B.I. Shklovskii, Phys. Rev. E **60**, 5802 (1999).
28. V.I. Perel, B.I. Shklovskii, Physica A **274**, 446 (1999).
29. T.T. Nguyen, A.Y. Grosberg, B.I. Shklovskii, Phys. Rev. Lett. **85**, 1568 (2000).
30. T.T. Nguyen, A.Y. Grosberg, B.I. Shklovskii, J. Chem. Phys. **113**, 1110 (2000).
31. T.T. Nguyen, I. Rouzina, B.I. Shklovskii, J. Chem. Phys. **112**, 2562 (2000).
32. T.T. Nguyen, B.I. Shklovskii, Phys. Rev. E **64**, 041407 (2001).
33. T.T. Nguyen, B.I. Shklovskii, Physica A **293**, 324 (2001).
34. A.A. Kornyshev, S. Leikin, Phys. Rev. Lett. **82**, 4138 (1999).
35. T.G. Dewey, Biopolymers **29**, 1793 (1990).
36. E. Rajasekaran, B. Jayaram, Biopolymers **34**, 443 (1994).
37. K. Sharp, Biopolymers **36**, 227 (1995).
38. K.A. Sharp, R.A. Friedman, V. Misra, J. Hecht, B. Honig, Biopolymers **36**, 245 (1995).
39. M.J. Stevens, Phys. Rev. Lett. **82**, 101 (1999).
40. M.C. Barbosa, M. Deserno, C.A. Holm, Europhys. Lett. **52**, 80 (2000).
41. J.J. Arenzon, J.F. Stilck, Y. Levin, Eur. Phys. J. B **12**, 79 (1999).
42. J.J. Arenzon, Y. Levin, J.F. Stilck, Physica A **283**, 1 (2000).
43. A. Diehl, H.A. Carmona, Y. Levin, Phys. Rev. E **64**, 011804 (2001).
44. M. Deserno, A. Arnold, C. Holm, Macromolecules **36**, 249 (2003).
45. H. Schiessel, P. Pincus, Macromolecules **31**, 7953 (1998).
46. P.L. Hansen, D. Svensek, V.A. Parsegian, R. Podgornik, Phys. Rev. E **60**, 1956 (1999).
47. R. Podgornik, P.L. Hansen, V.A. Parsegian, J. Chem. Phys. **113**, 9343 (2000).
48. P.L. Hansen, R. Podgornik, V.A. Parsegian, Phys. Rev. E **64**, 021907 (2001).
49. R. Golestanian, T.B. Liverpool, Phys. Rev. E **66**, 051802 (2002).

50. R. Golestanian, R. Kardar, T.B. Liverpool, Phys. Rev. Lett. **82**, 4456 (1999).
51. I. Borukhov, K.C. Lee, R.F. Bruinsma, W.M. Gelbart, A.J. Liu, M.J. Stevens, J. Chem. Phys. **117**, 462 (2002).
52. I. Borukhov, R.F. Bruinsma, W.M. Gelbart, A.J. Liu, Phys. Rev. Lett. **86**, 2182 (2001).
53. A.Y. Grosberg, T.T. Nguyen, B.I. Shklovskii, Rev. Mod. Phys. **74**, 329 (2002).
54. Y. Levin, Rep. Prog. Phys **65**, 1577 (2002).
55. W.M. Gelbart, R.F. Bruinsma, P.A. Pincus, V.A. Parsegian, Phys. Today **53**, September issue, 38 (2000).
56. C.P.K. Holm, R. Podgornik, *Electrostatic Effects in Soft Matter and Biophysics* (Dorcrecht, Kluwer, 2001).
57. G.S. Manning, Q. Rev. Biophys. **2**, 179 (1978).
58. R.W. Wilson, V.A. Bloomfield, Biochemistry **18**, 2192 (1979).
59. V.A. Bloomfield, R.W. Wilson, D.C. Rau, Biophys. Chem. **11**, 339 (1980).
60. J. Widom, R.L. Baldwin, J. Mol. Biol. **144**, 431 (1980).
61. I. Baeza, P. Gariglio, L.M. Rangel, P. Chavez, L. Cervantes, C. Arguello, C. Wong, C. Montanez, Biochemistry **26**, 6387 (1987).
62. P.G. Arscott, A.-Z. Li, V.A. Bloomfield, Biopolymers **30**, 619 (1990).
63. V.A. Bloomfield, Biopolymers **31**, 1471 (1991).
64. C. Ma, V.A. Bloomfield, Biophys. J. **19**, 234 (1994).
65. V.A. Bloomfield, Curr. Opin. Struct. Biol. **6**, 334 (1996).
66. V.A. Bloomfield, Biopolymers **44**, 269 (1997).
67. H. Deng, V.A. Bloomfield, J.M. Benevides, G.J. Thomas, Nucleic Acids Res. **28**, 3379 (2000).
68. H. Deng, V.A. Bloomfield, Biophys. J. **77**, 1556 (1999).
69. D.C. Rau, V.A. Parsegian, Biophys. J. **61**, 246 (1992).
70. R. Podgornik, D.C. Rau, V.A. Parsegian, Biophys. J. **66**, 962 (1994).
71. R. Marquet, C. Houssier, J. Biomol. Struct. Dyn. **9**, 159 (1991).
72. A.G. Moreira, R.R. Netz, Europhys. Lett. **52**, 705 (2000).
73. R.R. Netz, H. Orland, Eur. Phys. J. E **1**, 203 (2000).
74. A.W.C. Lau, D. Levine, P. Pincus, Phys. Rev. Lett. **84**, 4116 (2000).
75. A.W.C. Lau, P. Pincus, D. Levine, H.A. Fertig, Phys. Rev. E **63**, 051604 (2001).
76. A.W.C. Lau, D.B. Lukatsky, P. Pincus, S.A. Safran, Phys. Rev. E **65**, 051502 (2002).
77. A.W.C. Lau, P. Pincus, Phys. Rev. E **66**, 041501 (2002).
78. R. Kjellander, Ber. Buns. Ges. Phys. Chem. **100**, 894 (1996).
79. H. Greberg, R. Kjellander, J. Chem. Phys. **108**, 2940 (1998).
80. M. Deserno, F. Jiménez-Ängeles, C. Holm, M. Lozada-Cassou, J. Phys. Chem. B **105**, 10983 (2001).
81. J.X. Tang, P.A. Janmey, J. Biol. Chem. **271**, 8556 (1996).
82. J.X. Tang, S. Wong, P.T. Tran, P.A. Janmey, Ber. Buns. Ges. Phys. Chem. **100**, 796 (1996).
83. G.C.L. Wong, A. Lin, J.X. Tang, Y. Li, P.A. Janmey, C.R. Safinya, Phys. Rev. Lett. **91**, 018103 (2003).
84. I. Borukhov, R. Bruinsma, Phys. Rev. Lett. **87**, 158101 (2001).
85. J.C. Butler, T.E. Angelini, J.X. Tang, G.C.L. Wong, Phys. Rev. Lett. **91**, 028301 (2003).
86. H. Liang, T.E. Angelini, J. Ho, P.V. Braun, G.C.L. Wong, J. Am. Chem. Soc. **125**, 11786 (2003).
87. T.E. Angelini, H. Liang, W. Wriggers, G.C.L. Wong, Proc. Natl. Acad. Sci. U.S.A. **100**, 8634 (2003).
88. A. McGough, B. Pope, W. Chiu, A. Weeds, J. Cell. Biol. **138**, 771 (1997).
89. H. Richardsen, U. Vierl, G. Cevc, W. Fenzl, Europhys. Lett. **34**, 543 (1996).
90. R. Das, T.T. Mills, L.W. Kwok, G.S. Maskel, I.S. Millet, S. Doniach, K.D. Finkelstein, D. Herschlag, L. Pollack, Phys. Rev. Lett. **90**, 188103 (2003).
91. H. Lodish, A. Berk, S.L. Zipursky, P. Matsudaira, D. Baltimore, J. Darnell, *Molecular Cell Biology*, 4th ed. (Freeman, New York, 2000).
92. P. Sheterline, J. Clayton, J.C. Sparrow, *Actin* (Oxford University Press Inc., New York, 1998).
93. H.A. Al-Khayat, N. Yagi, J.M. Squire, J. Mol. Biol. **252**, 611 (1995).
94. T.T. Tibbits, D.L.D. Caspar, Acta. Cryst. A **49**, 532 (1993).
95. P.A. Janmey, J. Peetermans, K.S. Zaner, T.P. Stossel, T. Tanaka, J. Biol. Chem. **261**, 8357 (1986).
96. K.C. Holmes, D. Popp, W. Gebhard, W. Kabsch, Nature **347**, 44 (1990).
97. R.H. Coridan, T.E. Angelini, L.K. Sanders, W. Xian, G.C.L. Wong, unpublished results (2004).
98. E.H. Egelman, N. Francis, D.J. DeRosier, Nature **298**, 131 (1982).
99. U. Aebi, R. Millonig, H. Salvo, A. Engel, Ann. N.Y. Acad. Sci. **483**, 100 (1986).
100. Y. Tsuda, H. Yasutake, A. Ishijima, T. Yanagida, Proc. Natl. Acad. Sci. U.S.A. **93**, 12937 (1996).
101. J. Lee, E. Luijten, unpublished results (2004).
102. P.M. Chaikin, T.C. Lubensky, *Principles of Condensed Matter Physics* (Cambridge Univeristy Press, New York, 1995).
103. J. Als-Nielsen, J.D. Litster, R.J. Birgeneau, M. Kaplan, C.R. Safinya, A. Lindegaard-Andersen, S. Mathiesen, Phys. Rev. B **22**, 312 (1980).
104. G.C.L. Wong, W.H. de Jeu, H. Shao, K.S. Liang, R. Zentel, Nature **389**, 576 (1997).
105. C. Kittel, *Introduction to Solid State Physics* (Wiley, New York, 1966).
106. R.P. Feynman, *Statistical Mechanics; A Set of Lectures* (Reading, Mass., W.A. Benjamin, 1972).